



Rubin LSST Observing Strategies to Maximize Volume and Uniformity Coverage of Star-forming Regions in the Galactic Plane

Loredana Prisinzano¹ , Rosaria Bonito¹ , Alessandro Mazzi² , Francesco Damiani¹ , Sabina Ustamujic¹ , Peter Yoachim³ , Rachel Street⁴ , Mario Giuseppe Guarcello¹ , Laura Venuti⁵ , William Clarkson⁶ , Lynne Jones³ , and Leo Girardi⁷

¹ INAF–Osservatorio Astronomico di Palermo, Piazza del Parlamento, 1, I-90129, Palermo, Italy; loredana.prisinzano@inaf.it

² Dipartimento di Fisica e Astronomia Galileo Galilei, Università di Padova, Vicolo dell'Osservatorio 3, I-35122 Padova, Italy

³ Department of Astronomy, University of Washington, Box 351580, Seattle, WA 98195, USA

⁴ Las Cumbres Observatory, 6740 Cortona Drive, Suite 102, Goleta, CA 93117, USA

⁵ SETI Institute, 339 Bernardo Avenue, Suite 200, Mountain View, CA 94043, USA

⁶ Department of Natural Sciences, University of Michigan–Dearborn, 4901 Evergreen Road, Dearborn, MI 48128, USA

⁷ INAF–Osservatorio Astronomico di Padova, Vicolo dell'Osservatorio 5, I-35122 Padova, Italy

Received 2022 September 28; revised 2023 January 23; accepted 2023 February 16; published 2023 March 16

Abstract

A complete map of the youngest stellar populations of the Milky Way in the era of all-sky surveys is one of the most challenging goals in modern astrophysics. The characterization of the youngest stellar components is crucial not only for a global overview of the Milky Way's structure, of the Galactic thin disk, and its spiral arms, but also for local studies. In fact, the identification of star-forming regions (SFRs) and the comparison with the environment in which they form are also fundamental to put SFRs in the context of the surrounding giant molecular clouds and to understand still unknown physical mechanisms related to star and planet formation processes. In 10 yr of observations, the Vera C. Rubin Legacy Survey of Space and Time (Rubin LSST) will achieve an exquisite photometric depth that will allow us to significantly extend the volume within which we will be able to discover new SFRs and to enlarge the region of our own Galaxy we have detailed knowledge about. We describe here a metric that estimates the total number of young stars with ages $t < 10$ Myr and masses $> 0.3 M_{\odot}$ that will be detected with the Rubin LSST observations in the *gri* bands at a 5σ magnitude significance. We examine the results of our metric adopting the most recent simulated Rubin LSST survey strategies in order to evaluate the impact that different observing strategies might have on our science case.

Unified Astronomy Thesaurus concepts: Star clusters (1567); Interstellar medium (847); Milky Way Galaxy (1054); Young stellar objects (1834)

1. Introduction

In the era of all-sky astrophysical surveys, mapping the youngest stellar populations of the Milky Way in the optical bands is one of the main core science goals. Up to now, a full overall understanding of the Galactic components has been hampered by observational limits and, paradoxically, we have a better view of the morphological structure of external galaxies than of the Milky Way. In particular, it is crucial to trace the poorly known Galactic thin disk, and its spiral arms, where most of the youngest stellar populations are expected to be found.

The youngest Galactic stellar components are mainly found in star-forming regions (SFRs), namely stellar clusters and overdense structures originating from the collapse of molecular clouds, the coldest and densest part of the interstellar medium (Mac Low & Klessen 2004). It is by now relatively easy to identify in the near-, mid-, far-infrared (IR), and radio wavelengths the young stellar objects (YSOs) within SFRs during the first phases of the star formation process. In fact at these wavelengths, due to the presence of the optically thick infalling envelope or circumstellar disk around the central star, they show an excess with respect to the typical photospheric

emission. During the subsequent phases, they start to emit also in the optical bands, while the circumstellar disk is still optically thick (Bouvier et al. 2007). YSOs are no longer easily identifiable in the IR or at radio wavelengths, when the final dispersal of the disk material occurs and nonaccreting transition disks form (Ercolano et al. 2021). At these latter stages, a complete census of the YSOs can be achieved only using deep optical observations. Such a census is therefore crucial for a thorough comprehension of the large-scale three-dimensional structure of the young Galactic stellar component.

The identification of SFRs and the comparison with the environment in which they form are also fundamental to put them in the context of the surrounding giant molecular clouds and to answer still controversial open questions about the star formation process, such as (i) did the SFRs we observe originate from monolithic single star formation bursts or from multiple spatial and temporal scales, i.e., in a hierarchical mode (e.g., Kampakoglou et al. 2008)? (ii) When can the feedback from massive stars affect protoplanetary disk evolution (Tanaka et al. 2018) or trigger subsequent star formation events, as thought happened, for example, for the supernova explosion in the λ Ori region (Kounkel et al. 2020)? (iii) Is the overall spatial distribution of SFRs correlated to an overall large-scale structure, such as the Gould Belt or the damped wave, very recently suggested by Alves et al. (2020)?

The Vera C. Rubin Observatory (Rubin; Ivezić 2019) will conduct a Legacy Survey of Space and Time (LSST) with a



Original content from this work may be used under the terms of the [Creative Commons Attribution 4.0 licence](https://creativecommons.org/licenses/by/4.0/). Any further distribution of this work must maintain attribution to the author(s) and the title of the work, journal citation and DOI.

very impressive combination of flux sensitivity, area, and temporal sampling rate (Bianco et al. 2022).

A flexible scheduling system is designed to maximize the scientific return under a set of observing constraints. Rubin will perform a set of surveys over 10 yr. These include the Wide–Fast–Deep (WFD) survey, which is the “main” LSST survey, primarily focused on low-extinction regions of the sky for extragalactic science; and the Deep Drilling Fields, which are a set of a few individual fields that will receive high-cadence and additional “minisurveys” that cover specific sky regions such as the ecliptic plane, Galactic plane (GP), and the Large and Small Magellanic Clouds with specific observing parameters (Bianco et al. 2022).

The implementation of the Rubin LSST observing strategy must meet the basic LSST Science Requirements,⁸ but significant flexibility in the detailed cadence of observations is left to ensure the best optimization of the survey. The scientific community has been involved in giving feedback on specific science cases on the distribution of visits within a year, the distribution of images between filters, and the definition of a “visit” as single or multiple exposures. To this aim, simulated realizations of the 10 yr sequence of observations acquired by LSST, for different sets of basis functions that define the different survey strategies, indicated as OpSim, are made available to the community. Such simulated observations can be analyzed through an open-access software package, the metrics analysis framework (MAF; Jones et al. 2014), where specific metrics can be calculated to quantify the suitability of a given strategy for reaching a particular science objective.

In the original baseline, i.e., the reference benchmark survey strategy, the minisurvey of the GP was covered by a number of visits a factor ~ 5 smaller than those planned for WFD. The main reason for this choice is to avoid highly extincted regions with $E(B - V) > 0.2$, since this amount of dust extinction is problematic for extragalactic science, as suggested by Jones et al. (2021). Nevertheless, mapping the Milky Way is one of the four broad science pillars that LSST will address (Bianco et al. 2022).

We aim to show here that alternative implementations in which the number of visits planned for the WFD survey is extended also to the Galactic thin disk ($|b| \lesssim 5^\circ - 10^\circ$) will significantly increase the impact of Rubin LSST on the understanding of the Galactic large-scale structures and, in particular, of the large molecular clouds in which stars form. The stellar components of the SFRs, and, in particular, the most populated low-mass components down to the M-dwarf regime with age $t \lesssim 10$ Myr that will be discovered with Rubin LSST observations, are one of the most relevant outputs of the star formation process. Assessing their properties (spatial distribution in the Galaxy, masses, ages, and age spread) is crucial for tracing the global structure of the youngest populations as well as pinpointing several underdebated disputes such as the universality of the initial mass function (IMF), the duration of the evolutionary phases involved in the star formation process, and the dynamical evolution (Chabrier 2003; Tassis & Mouschovias 2004; Ballesteros-Paredes et al. 2007; Parker et al. 2014).

Even though the thin disk of the Galaxy is strongly affected by high dust extinction and crowding issues, it is the only

Galactic component where most of the structures are found and where young stars are exclusively found.

A big step forward has been made regarding the comprehension of Galactic components thanks to the Gaia data that allows us to achieve a clearer and more homogeneous overview of the Galactic structures, including the youngest ones, but at distances from the Sun limited to 2–3 kpc (Zari et al. 2018; Kounkel & Covey 2019; Kounkel et al. 2020; Kerr et al. 2021; Prisinzano et al. 2022). The exquisite science return from the very deep Rubin LSST static photometry, derived from coadded images, is the only opportunity to push such large-scale studies of young stars into otherwise unreachable and unexplored regions.

With respect to the old open clusters, the study of the SFRs is favored by the intrinsic astrophysical properties of the low-mass YSOs, representing the bulk of these populations. In fact, during the pre-main-sequence (PMS) phase, M-type young stars are more luminous in bolometric light than the stars of the same mass in the main sequence (MS) phase. For example, for a given extinction, a 1 Myr (10 Myr) old $0.3 M_\odot$ star is 3.4 mag (1.6 mag) brighter than a 100 Myr star of the same mass (Prisinzano et al. 2018b; Tognelli et al. 2018). Therefore, if on one hand the extinction limits our capability to detect such low-mass stars, on the other hand, the higher intrinsic luminosity of young stars ($t < 10$ Myr) compensates for this effect, allowing for a significant increase in the volume of PMS stars detectable with respect to old MS stars. Such a property has been exploited in Damiani (2018), Prisinzano et al. (2018a), and Venuti et al. (2019), where a purely photometric approach using *gri* magnitudes combined with the most deep near-IR magnitudes available in the literature has been adopted to statistically identify YSOs at distances where M-type MS stars are no longer detectable, because they are intrinsically less luminous than the analogous M-type PMS stars.

We note, however, that studies of other relevant structures, such as stellar clusters as tracers of the Galactic chemical evolution (Prisinzano et al. 2018a), for example, as well as transient phenomena (see Bonito et al. 2023, Street et al. 2023) would also benefit from the observed strategy discussed in this paper.

The goal of this paper is to evaluate the impact on the YSO science of different Rubin LSST observing strategies and, in particular, of the different WFD-like cadences extended to the GP, as an improvement with respect to the baseline observing strategy.

2. Metric Definition

The metric we present in this work is defined as the number of detectable YSOs with masses down to $0.3 M_\odot$ and ages $t \leq 10$ Myr, distributed in the GP and, in particular, in the thin disk of the Milky Way.

The number of YSOs estimated in this work is not based on empirical results but on the theoretical description of the star number density ρ (number of stars per unit volume) in the Galactic thin disk, integrated within the volume accessible with Rubin LSST observations. In particular, the total number of young stars observable within a given solid angle Ω around a direction (e.g., a Healpix) defined by the Galactic coordinates (l, b) will be obtained by integrating such density along cones,

⁸ <https://docushare.lsst.org/docushare/dsweb/Get/LPM-17>

using volume elements

$$dV = \Omega r^2 dr, \quad (1)$$

where r is the distance from the Sun. Therefore we define this number of stars as

$$N(<r_{\max}) = \int_0^{r_{\max}} \rho(r, l, b) dV, \quad (2)$$

where r_{\max} is the maximum distance from the Sun that is defined from the observation depth.

2.1. Density Law of YSOs in the Galactic Thin Disk

In the Galactic thin disk, the star density distribution or number density, usually called the density profile or density law, can be described by a double exponential (e.g., Cabrera-Lavers et al. 2005), as follows:

$$\rho(r, l, b) = A \times \exp\left(-\frac{r|\sin b|}{h} - \frac{R}{r_1}\right), \quad (3)$$

where A is the total density normalization (to be computed below), h is the thin-disk scale height that we assume equal to 300 pc (Bland-Hawthorn & Gerhard 2016), R is the Galactocentric distance, and r_1 is the thin-disk radial scale length that we assume equal to 2.6 kpc (Freudenreich 1998). The Galactocentric distance R can be expressed in terms of r , l , and Galactic Center distance from the Sun D , as

$$R = \sqrt{(D - r \cos l)^2 + (r \sin l)^2}. \quad (4)$$

To derive the density normalization constant A , we integrate the thin-disk density ρ over the whole Galaxy, to obtain the total number of stars as

$$N = 4\pi A h r_1^2. \quad (5)$$

Recent results by Giammaria et al. (2021, see their Table 2) show that, within a factor of 2, we can assume in the Galaxy a constant star formation rate. Therefore, in the whole Galaxy the total number of stars with ages $t < 10$ Myr, N_{yng} , can be estimated as

$$N_{\text{yng}} = \frac{t_{\text{yng}}}{t_{\text{MW}}} \times N_{\text{tot}}, \quad (6)$$

where $t_{\text{yng}} = 10$ Myr is the upper age limit for the youngest stellar component considered here, t_{MW} is the Galaxy age that we assume to be ~ 10 Gyr, and N_{tot} is the total number of the stars in the Galaxy, roughly equal to 10^{11} . With these assumptions N_{yng} amounts to 10^8 stars. Moreover, to take into account that we are going to miss about 20% of the IMF below $0.3 M_{\odot}$ (Weidner et al. 2010), we should add a corrective factor of 0.8 for the number of actually observable stars.

Therefore, we may reasonably approximate in Equation (5) for the total thin-disk content $N \sim 0.8 \times N_{\text{yng}}$, from which $A \sim \frac{0.8 \times 10^8}{4\pi h r_1^2}$, to be used in Equation (3).

2.2. Rubin LSST Accessible Volume

The element of volume within a given solid angle Ω , as well as the density law ρ , defined by Equations (1) and (3), respectively, depends on the distance from the Sun. At a given mass and age and for a given extinction, the maximum distance that can be achieved with Rubin LSST data is a function of the photometric observational depth and thus of the adopted observing strategy. To evaluate such a distance, and thus to define such a volume, our metric has been defined with the following criteria:

1. use of the Rubin LSST *gri* filters, assuming the use of the $r - i$ versus $g - r$ diagram to photometrically select the YSOs, as in Damiani (2018), Prisinzano et al. (2018a), and Venuti et al. (2019). This is a restrictive assumption, since more than three Rubin LSST filters will be used for the selection;
2. use of a dust map to take into account the nonuniform extinction pattern that characterizes the GP, in particular toward the Galactic Center;
3. estimate the maximum distance that will be achieved assuming different OpSims.

The definition of the metric is therefore based on the following rationale: specify the desired accuracy magnitude/ $\sigma = 5$ for *gri* filters and compute the corresponding limiting magnitudes from coadded images; correct for extinction the apparent magnitudes using a dust map; compute the maximum distance at which a 10 Myr old star of $0.3 M_{\odot}$ can be detected, assuming the absolute magnitudes in the *gri* filters, $M_g = 10.32$, $M_r = 9.28$, and $M_i = 7.97$, predicted for such a star by a 10 Myr solar metallicity isochrone (Tognelli et al. 2018); calculate the corresponding volume element within a $N_{\text{side}} = 64$ Healpix; and integrate the young star density within the volume element, through Equation (2).

2.2.1. Dust Map

Dust extinction is an increasing function of distance; nearby stars are then affected by $E(B - V)$ values smaller than those of more distant stars. The Schlegel et al. (1998) map has an important use in astronomy, but provides an integrated extinction along a line of sight at the maximum distance corresponding to the adopted $100 \mu\text{m}$ observations. As a consequence, it is more useful for extragalactic studies (Amôres et al. 2021). Assuming a 2D dust extinction i.e., a map that depends only on the positions (e.g., the Galactic coordinates l, b) leads to a significant overestimation of the real extinction at different distances, especially in the directions with $A_V > 0.5$ (e.g. Arce & Goodman 1999; Amôres & Lépine 2005), such as in the GP and, in particular, in the Galactic spiral arms.

In recent years, many efforts have been made to derive 3D extinction maps that take into account the strong dependence on the distance, as summarized in Amôres et al. (2021).

A 3D dust map, appropriated for the Rubin LSST metrics, has been developed (A. Mazzi et al. in preparation) by using the Lallement et al. (2019) map, the `mw dust`. Combined19 map, based on the Drimmel et al. (2003), Green et al. (2019), and Marshall et al. (2006) maps, combined with the method described in Bovy et al. (2016), and the Planck Collaboration et al. (2016) map Planck. The 3D map has been integrated in the MAF as `DustMap3D` to distinguish it from the default

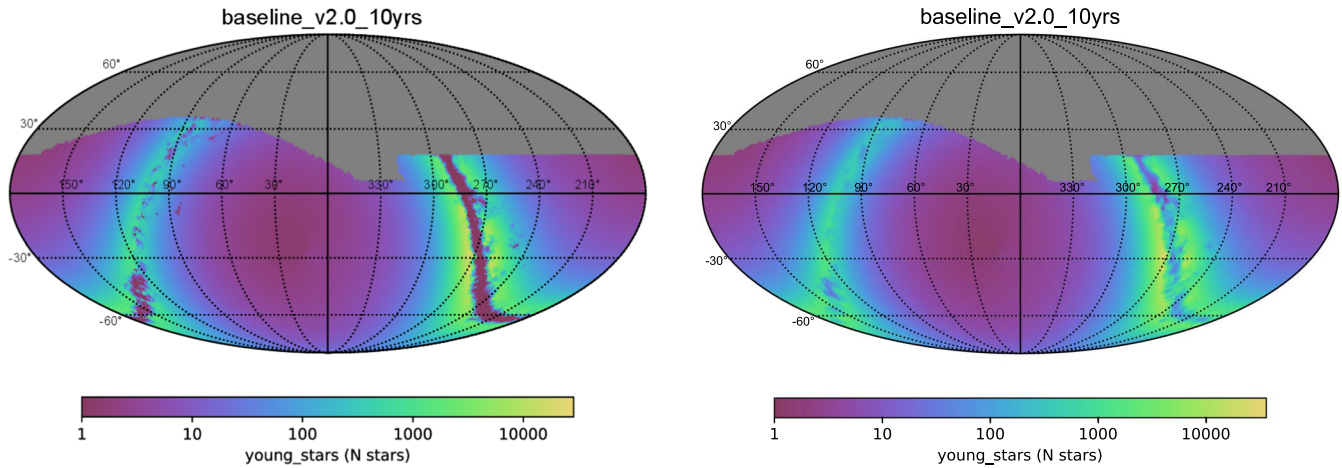


Figure 1. Map of the number of detectable YSOs per HEALPix computed with our metric, using the 2D dust map (left panel) and the 3D dust map (right panel). In both cases the `baseline_v2.0_10yr` has been adopted. The sky is shown in the equal-area Mollweide projection in equatorial coordinates and the HEALPix grid resolution is $N_{\text{side}} = 64$.

Rubin 2D Dust_values based on the Schlegel et al. (1998) map. The two maps can be imported into the MAF with the following commands:

```
from rubin_sim.photUtils import Dust_values
from rubin_sim.maf.maps import DustMap3D.
```

To test the effect on our metric of using the 2D or the 3D dust map and to select the one predicting the more realistic results, we computed our metric by considering the default 2D dust map implemented within the MAF, as well as the new 3D dust map. Figure 1 (left panel) shows the results of our metric on the OpSim simulation named `baseline_v2.0_10yr`, obtained by assuming the 2D dust map, while Figure 1 (right panel) shows the corresponding result, assuming the 3D dust map.

The results point out that by assuming the 3D distance-dependent extinction map, the number of detectable YSOs decreases only smoothly toward the inner GP. On the contrary, the sharp decrease in the detected YSOs in the inner GP is evidence of an unrealistic star distribution due to the adoption of an unsuitable overestimated extinction map (2D dust map). Therefore, the final version of the code defining our metric includes the 3D dust map.

2.2.2. Crowding Effects

Our metric has been defined by assuming the formal limiting magnitude at 5σ photometric precision, however in several wide areas of the GP, the limiting magnitude should be set by the photometric errors due to the crowding. To take into account such an effect a specific crowding metric has been developed within the MAF based on the TRILEGAL stellar density maps (Dal Tio et al. 2022) to compute the errors that will result from stellar crowding.⁹

Such a crowding metric has been included in our code since we expect that the observations become severely incomplete when the photometric errors due to the crowding exceed 0.25 mag. These photometric errors are derived using the formalism by Olsen et al. (2003) and the 0.25 mag criterion has been empirically checked using deep observations of the bulge (W.

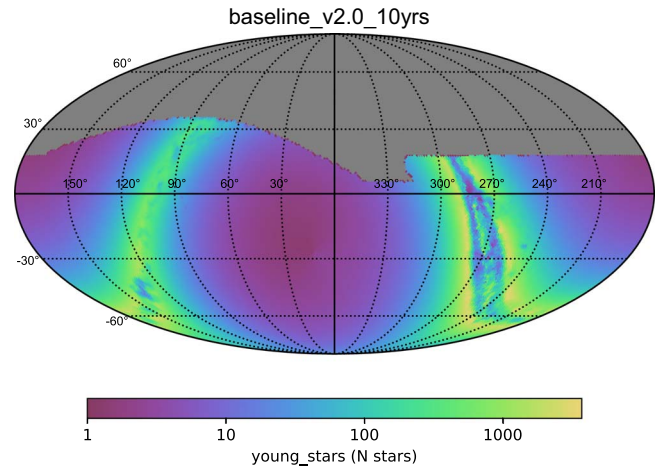


Figure 2. Map of the number of detectable YSOs per HEALPix computed with our metric, using the `baseline_v2.0_10yr`, the 3D dust map and the crowding metric. The sky is shown in the equal-area Mollweide projection in equatorial coordinates and the HEALPix grid resolution is $N_{\text{side}} = 64$.

Clarkson et al. 2023, in preparation). Therefore, to detect the faintest stars in very crowded regions we used the minimum (brightest) magnitude between those obtained with `maf.Coaddm5Metric()` and `maf.CrowdingM5Metric(crowding_error=0.25)`.

The limiting magnitudes achieved after including the crowding effects can be ~ 2 – 3 mag brighter than those obtained without considering confusion effects. As a consequence, the number of YSOs detected by including the confusion metric, shown in Figure 2, can be significantly smaller than that predicted by the metric that does not include such an effect, shown in Figure 1, right panel.

We note that the two-pronged fork feature in the map shown in Figure 2 is due to the fact that in the layers immediately above and below the GP, the crowding is the dominant effect and the number of possible detections goes down here from more than 10,000 to surprisingly low values of 10–100 (sources/HEALPix). On the contrary, in the central layer of the GP, the extinction is the dominant effect, while the crowding effect is negligible since a smaller number of stars is visible. As a consequence, after applying the crowding metric, the number of detections in this central layer remains almost

⁹ https://github.com/LSST-nonproject/sims_maf_contrib/blob/master/science/static/Crowding_tri.ipynb.

constant (around 1000 sources),¹⁰ while the missed detection fraction is significantly larger in the layers immediately higher and lower than the GP. This result is consistent with what recently pointed out by Cantat-Gaudin et al. (2023) for the Gaia data.

3. Results

The Python code that computes the metric described in the previous sections is publicly available in the central `rubin_sim` MAF metrics repository with the name `YoungStellarObjectsMetric.py`.¹¹

To evaluate the impact of the different family sets of OpSim on our science case, we considered the current state of LSST v2.0 and v2.1 OpSim databases and metric results.¹² In particular, we considered the following runs:

1. `baseline_v2.0_10yr`, the reference benchmark survey strategy in which the WFD survey footprint has been extended to include the central GP and bulge, and is defined by low-extinction regions. Such a configuration includes also five DDFs and the additional minisurvey areas of the North Ecliptic Plane, the GP, and the South Celestial Pole.
2. `baseline_v2.1_10yr`, in which the Virgo cluster and the requirement on the seeing $\text{FWHM}_{\text{Eff}} < 0''.8$ for the images in the r and i bands have been added with respect to the `baseline_v2.0_10yr`.
3. A varied GP (“Vary GP”) family of simulations in which the fraction of the amount of survey time spent on covering the background (non-WFD-level) GP area ranges from 0.01 to 1.0 (labeled as `frac0.01–frac1.00`), where 1.0 corresponds to extending the WFD cadence to the entire GP. The baseline characteristics, including the ratio of visits over the remainder of the footprint, are kept the same. In our case, we considered the `vary_gp_gfrac1.00_v2.0_10yr` survey, planning the maximum amount of time on the GP.
4. Plane Priority, the family of OpSim that uses the GP priority map, contributed to by the LSST Stars, Milky Way, and Local Volume and Transients and Variable Stars science collaborations, as the basis for further variations on GP coverage. For this family of simulations, different levels of priority of the GP map are covered at WFD level, unlike the baseline and Vary GP family where only the bulge area is covered at the WFD level. In our case, we considered the `plane_priority_priority0.3_pbt_v2.1_10yr` survey, since it maximizes the results of our metric.

To evaluate the best observing strategy to be adopted for the YSO science, we defined as a figure of merit (FoM) the ratio between the number of young stars detected with a given OpSim with respect to the number of young stars detected with the `baseline_v2.0_10yr` survey, the latter taken as a reference. The map of the number of visits planned for these four representative OpSim surveys is shown in Figure 3, while the results of the metric, i.e., the number of YSOs with ages $t < 10$ Myr and masses $> 0.3 M_{\odot}$ obtained with these four

representative OpSim surveys are given in Table 1 and shown in Figure 4. The FoM obtained with our metric using the four OpSim described before are also given in Table 1. The number of YSOs and the FoM predicted by the metrics, both including and not including the crowding effects, are given in order to quantify the differences due to the confusion effects.

4. Discussion and Conclusions

In this paper we presented a metric aimed at estimating the number of YSOs we can discover with Rubin LSST static science data. To take into account the effects due to extinction, we evaluated the metric by using both the default LSST MAF 2D dust map and the 3D dust map where a more realistic dependence on the distance is included. The results of this comparison show that the 2D dust map overestimates $E(B - V)$ values for closely (few kiloparsecs) accessible stars, even in the direction of the GP. For this reason, the final metric has been implemented by considering the 3D dust map integrated into the MAF.

To evaluate the faintest magnitudes that can be attained in crowded regions, a specific crowding metric has been imported in the code. In order to quantify the crowding effects, we evaluated our metric by also neglecting the crowding effects. The results show that, if the crowding metric is included, the number of detected YSOs (N_{Crow} in Table 1) is a factor 0.6–0.63 smaller than the number of YSOs predicted if the crowding is not considered (column N in Table 1). Since the most realistic predictions are those obtained by including the crowding effects, the final version of the code that defines the YSO metric includes the crowding metric.

The impact of changing from the baseline v2.0 to v2.1 is negligible, and while adopting the `vary_gp_gfrac1.00_v2.0_10yr` survey, the only one available covering 100% of the GP with WFD exposure times, the predicted number of YSOs ($t < 10$ Myr) down to $0.3 M_{\odot}$ is a factor 1.15 larger than that predicted adopting the `baseline_v2.0_10yr`, leading to a gain of 0.74×10^6 newly discovered YSOs at very large distances. An even higher impact can be obtained by adopting the most recently contributed `plane_priority_priority0.3_pbt_v2.1_10yr` predicting different levels of priority of the GP map. With this survey, the predicted number of YSOs is a factor 1.24 higher with respect to the baseline, corresponding to a gain of $\sim 1.17 \times 10^6$ additional YSOs.

To determine at what distance and beyond which distance from the Sun this gain is most significant, we also included in our metric the computation of the maximum distance that can be reached for a 10 Myr old star of $0.3 M_{\odot}$ within each HEALpix. We derived the distribution of such distances, weighted by the number of YSOs that can be detected in each line of sight. The distributions obtained for the four OpSim considered in this work are shown in Figure 5.

We note that the number of YSOs detected at distances from the Sun larger than ~ 10 kpc is significantly larger for the OpSim `plane_priority_priority0.3_pbt_v2.1_10yr` and `vary_gp_gfrac1.00_v2.0_10yr` than for the two baselines. The curve of the `vary_gp_gfrac1.00_v2.0_10yr` OpSim sits below the baseline curves for $d = 7$ – 10 kpc. This could be due to the fact that in the two baselines, the number of visits in the regions outside the GP is higher (800–900) with respect to that planned for the `vary_gp_gfrac1.00_v2.0_10yr` (700–800), where the coverage is uniform. This comparison clearly shows that the

¹⁰ Note the different color scales in the maps.

¹¹ https://github.com/lst/rubin_sim/blob/main/rubin_sim/maf/maf_contrib/young_stellar_objects_metric.py

¹² <http://astro-lsst-01.astro.washington.edu:8080>.

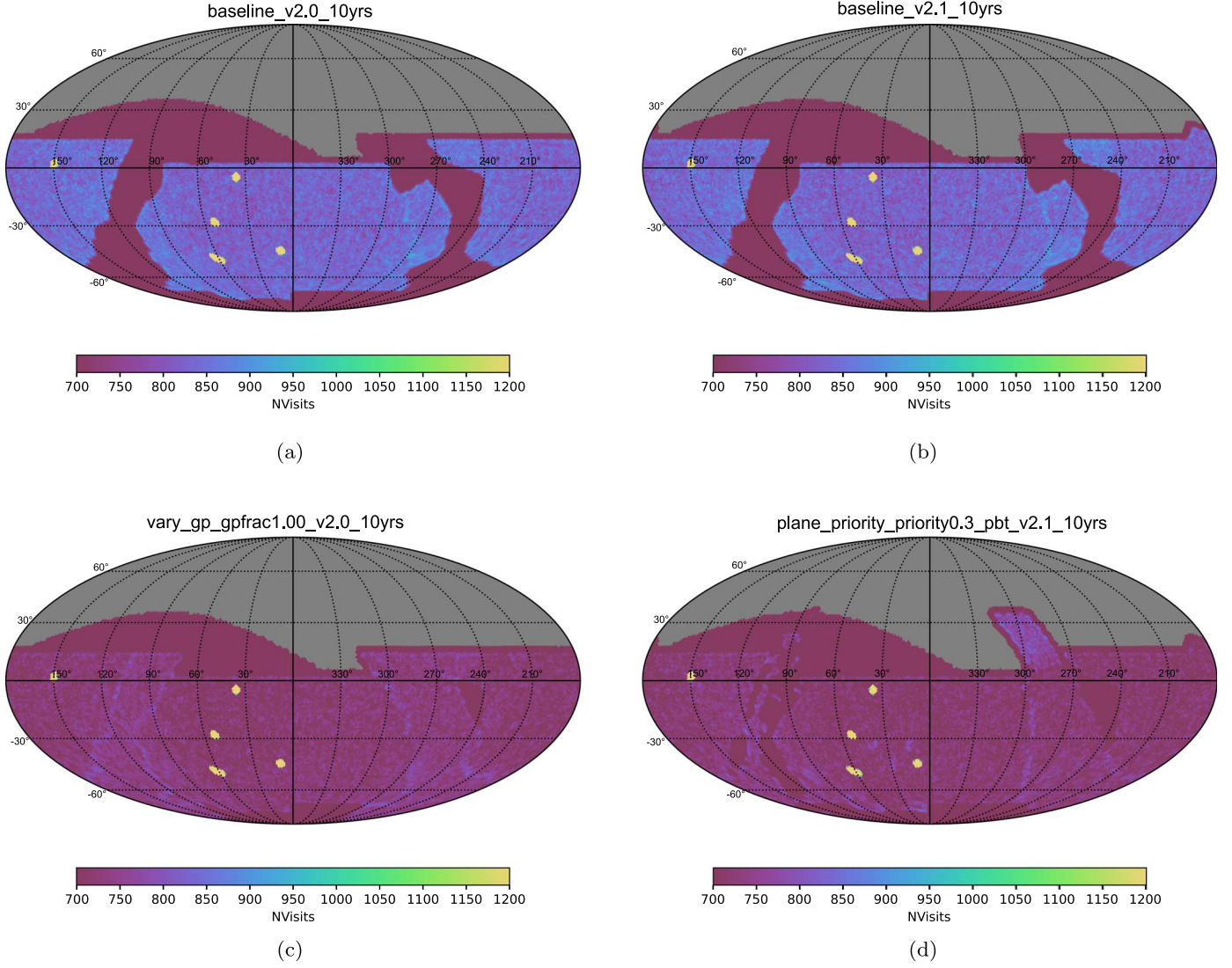


Figure 3. Map of the number of visits per HEALPix planned for the four representative OpSim relevant for our science case. The small yellow patches are the Deep Drilling Fields (DDFs) to which a higher number of observations is assigned. Note the Rubin LSST footprint of the baselines (panels (a) and (b)) is significantly different with respect to that of the `vary_gp_gpfrac1.00_v2.0_10yr` and the `plane_priority_priority0.3_pbt_v2.1_10yr` OpSim (panels (c) and (d)), where the number of visits at the WFD level is also assigned to the high dust extinction GP area. The sky is shown in the equal-area Mollweide projection in equatorial coordinates and the HEALPix grid resolution is $N_{\text{side}} = 64$.

Table 1

Number of YSOs with Ages $t < 10$ Myr and Masses $> 0.3 M_{\odot}$ that can be Detected at Distances $< r_{\text{max}}$ Set by Different OpSim Surveys, and Relative FoM Values

OpSim ID	N	FoM	N_{Crow}	FoM_{Crow}
<code>baseline_v2.0_10yr</code>	8.08×10^6	1.00	4.84×10^6	1.00
<code>baseline_v2.1_10yr</code>	8.10×10^6	1.00	4.87×10^6	1.01
<code>vary_gp_gpfrac1.00_v2.0_10yr</code>	8.92×10^6	1.10	5.58×10^6	1.15
<code>plane_priority_priority0.3_pbt_v2.1_10yr</code>	9.51×10^6	1.18	6.02×10^6	1.24

Note. Estimated by both neglecting the crowding metric (N and FoM columns) and by including them (N_{Crow} and FoM_{Crow} columns).

science enabled by adopting an observing strategy consistent with the `plane_priority_priority0.3_pbt_v2.1_10yr` or `vary_gp_gpfrac1.00_v2.0_10yr` OpSims would be precluded if we followed the prescriptions of other simulations. These results highlight the great impact of the Rubin LSST data, when the WFD cadence is extended to the GP. This is mainly due to the large number of very far young stars that will be discovered. We note that the two baselines and the `vary_gp_gpfrac1.00_v2.0_10yr` OpSims

show an asymmetric distribution with a peak that is around 9 kpc and 14 kpc, respectively. The `plane_priority_priority0.3_pbt_v2.1_10yr` OpSim shows a more smoothed and symmetric shape, which is likely due to the different levels of priority given to the GP for this survey strategy.

We remark that a gain of 24% in the number of discovered YSOs, mainly arising at distances larger than 10 kpc, represents a strong justification to extend the WFD strategy to the GP, and to ensure the uniformity of the observing strategy in the Galaxy.

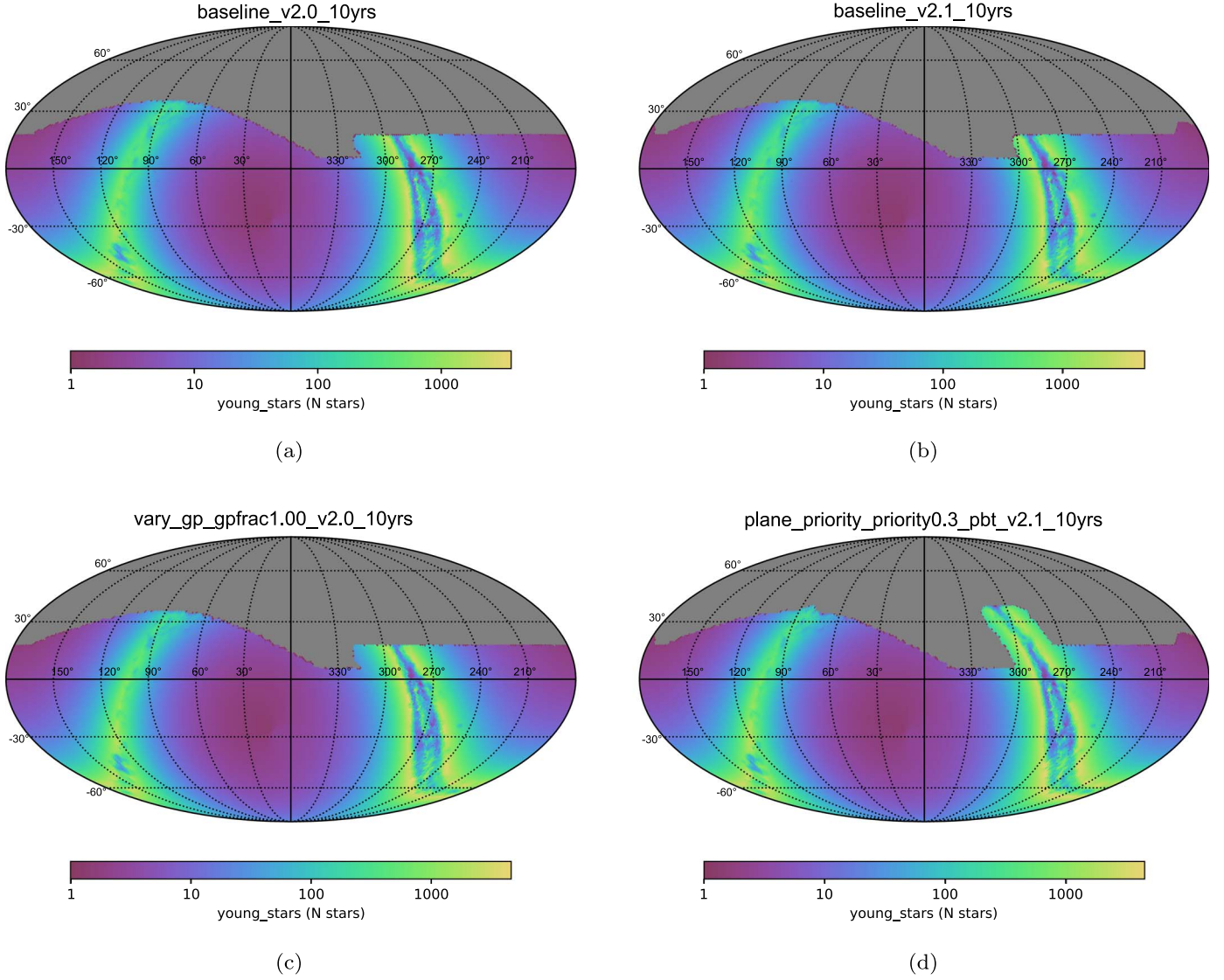


Figure 4. Map of the number of YSOs per HEALPix as computed by our metric, adopting the OpSim surveys listed in Table 1 and indicated by the names superimposed on top of each panel. The sky is shown in the equal-area Mollweide projection in equatorial coordinates and the HEALPix grid resolution is $N_{\text{side}} = 64$. Note that the map in panel (a) is identical to the map shown in Figure 2.

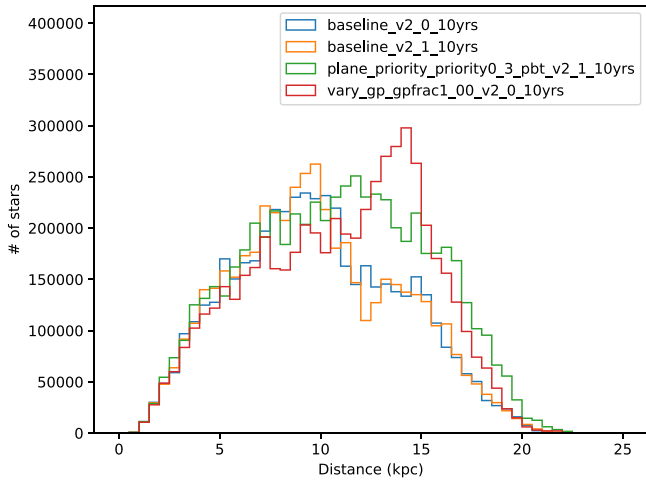


Figure 5. Number of detected YSOs as a function of the distance for the four OpSim indicated in Table 1.

Finally, we note that our metric scales more strongly with the area rather than with the number of visits per pointing and therefore, in case the `plane_priority_priority0.3_pbt_v2.1_10yr` survey cannot be adopted, we advocate the adoption of the `vary_gp_gpfrac1.00_v2.0_10yr`, to preserve the uniform coverage of the GP.








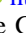




We stress that our request is to extend the number of visits planned for the WFD to the GP but without constraints on the temporal observing cadence, since our analysis is based on the use of the coadded *gri* Rubin LSST images. However, different visits per night should be in different filters from the *gri* set. The same applies in case two or three visits per night are made, as this would enhance the number but also the accuracy of color measurements available, and hence heighten the fraction of YSOs that can be detected and characterized thanks to their color properties. The color accuracy is improved if the observations in different filters are taken close together in time and therefore least affected by star variability.

The metric described in this work has been developed assuming the use of a photometric technique to statistically identify YSOs mainly expected within SFRs as already done in Damiani (2018), Prisinzano et al. (2018a), and Venuti et al. (2019). However, YSOs can also form dispersed populations, mingled with the general thin-disk population (e.g., Briceño et al. 2019; Luhman 2022), and their identification can be hampered by the strong field-star contamination. Such an issue can be overcome by also exploiting Rubin LSST's accurate proper-motion and parallax measurements (Marshall et al. 2017; Prisinzano et al. 2018b), as well as the most deep photometric near-IR photometric surveys, such as, for example, the VISTA Variables in the Via Lactea (Minniti et al. 2010). Nevertheless, a spectroscopic follow-up will be needed for a full characterization of the YSOs detected with Rubin LSST, for which spectroscopic data can be achieved. Forthcoming spectroscopic facilities like WEAVE (Dalton et al. 2020) and 4MOST (de Jong et al. 2022) will be crucial to this aim, at least within the limiting magnitudes they can achieve.

The exquisite depth of the Rubin LSST coadded images represents a unique opportunity to study large-scale young structures and to investigate the low-mass stellar populations in/around the thin-disk GP, where star formation mainly occurs. Our results suggest that in order to maximize the volume of detected YSOs and the uniformity of coverage of the large-scale young structures, the amount of survey time dedicated to the GP should be equal to or comparable to the WFD level. These observations will allow us to better characterize the Galactic structure and in particular the Norma, Scutum, Sagittarius, Local, Perseus and the Outer spiral arms, reported in Reid et al. (2014).

This work was supported by the Preparing for Astrophysics with LSST Program, funded by the Heising-Simons Foundation through grant 2021-2975, and administered by Las Cumbres Observatory. A.M. acknowledges financial support from Padova University, Department of Physics and Astronomy Research Project 2021 (PRD 2021). L.V. is supported by the National Aeronautics and Space Administration (NASA) under grant No. 80NSSC21K0633 issued through the NNH20ZDA001N Astrophysics Data Analysis Program (ADAP). The authors thank the anonymous referee for the comments that improved the quality of the manuscript.

ORCID iDs

Loredana Prisinzano  <https://orcid.org/0000-0002-8893-2210>
 Rosaria Bonito  <https://orcid.org/0000-0001-9297-7748>
 Alessandro Mazzi  <https://orcid.org/0000-0002-7503-5078>
 Francesco Damiani  <https://orcid.org/0000-0002-7065-3061>
 Sabina Ustamujic  <https://orcid.org/0000-0003-4596-2628>
 Peter Yoachim  <https://orcid.org/0000-0003-2874-6464>
 Rachel Street  <https://orcid.org/0000-0001-6279-0552>
 Mario Giuseppe Guarcello  <https://orcid.org/0000-0002-3010-2310>
 Laura Venuti  <https://orcid.org/0000-0002-4115-0318>
 William Clarkson  <https://orcid.org/0000-0002-2577-8885>
 Lynne Jones  <https://orcid.org/0000-0001-5916-0031>
 Leo Girardi  <https://orcid.org/0000-0002-6301-3269>

References

- Alves, J., Zucker, C., Goodman, A. A., et al. 2020, *Natur*, **578**, 237
 Amôres, E. B., Jesus, R. M., Moitinho, A., et al. 2021, *MNRAS*, **508**, 1788
 Amôres, E. B., & Lépine, J. R. D. 2005, *AJ*, **130**, 659
 Arce, H. G., & Goodman, A. A. 1999, *ApJL*, **512**, L135
 Ballesteros-Paredes, J., Klessen, R. S., Mac Low, M.-M., & Vazquez-Semadeni, E. 2007, in *Protostars and Planets V*, ed. B. Reipurth et al. (Tucson, AZ: Univ. Arizona Press), 63
 Bianco, F. B., Ivezić, Ž., Jones, R. L., et al. 2022, *ApJS*, **258**, 1
 Bland-Hawthorn, J., & Gerhard, O. 2016, *ARA&A*, **54**, 529
 Bonito, R., Venuti, L., Ustamujic, S., et al. 2023, *ApJS*, **265**, 27
 Bouvier, J., Alencar, S. H. P., Harries, T. J., Johns-Krull, C. M., & Romanova, M. M. 2007, in *Protostars and Planets V*, ed. B. Reipurth, D. Jewitt, & K. Keil (Tucson, AZ: Univ. Arizona Press), 479
 Bovy, J., Rix, H.-W., Green, G. M., Schlafly, E. F., & Finkbeiner, D. P. 2016, *ApJ*, **818**, 130
 Briceño, C., Calvet, N., Hernández, J., et al. 2019, *AJ*, **157**, 85
 Cabrera-Lavers, A., Garzón, F., & Hammersley, P. L. 2005, *A&A*, **433**, 173
 Cantat-Gaudin, T., Founesneau, M., Rix, H.-W., et al. 2023, *A&A*, **669**, A55
 Chabrier, G. 2003, *PASP*, **115**, 763
 Dal Tio, P., Pastorelli, G., Mazzi, A., et al. 2022, *ApJS*, **262**, 22
 Dalton, G., Trager, S., Abrams, D. C., et al. 2020, *Proc. SPIE*, **11447**, 1144714
 Damiani, F. 2018, *A&A*, **615**, A148
 de Jong, R. S., Bellido-Tirado, O., Brynnel, J. G., et al. 2022, *Proc. SPIE*, **12184**, 1218414
 Drimmel, R., Cabrera-Lavers, A., & López-Corredoira, M. 2003, *A&A*, **409**, 205
 Ercolano, B., Picogna, G., Monsch, K., Drake, J. J., & Preibisch, T. 2021, *MNRAS*, **508**, 1675
 Freudenreich, H. T. 1998, *ApJ*, **492**, 495
 Giammaria, M., Spagna, A., Lattanzi, M. G., et al. 2021, *MNRAS*, **502**, 2251
 Green, G. M., Schlafly, E., Zucker, C., Speagle, J. S., & Finkbeiner, D. 2019, *ApJ*, **887**, 93
 Ivezić, Ž. 2019, *ApJ*, **873**, 111
 Jones, R. L., Yoachim, P., Chandrasekharan, S., et al. 2014, *Proc. SPIE*, **9149**, 91490B
 Jones, R. L., Yoachim, P., Ivezić, Z., Neilsen, E., & Ribeiro, T. 2021, Survey Strategy and Cadence Choices for the Vera C. Rubin Observatory Legacy Survey of Space and Time (LSST), <https://pstn-051.lsst.io/>
 Kampakoglou, M., Trotta, R., & Silk, J. 2008, *MNRAS*, **384**, 1414
 Kerr, R. M. P., Rizzuto, A. C., Kraus, A. L., & Offner, S. S. R. 2021, *ApJ*, **917**, 23
 Kounkel, M., & Covey, K. 2019, *AJ*, **158**, 122
 Kounkel, M., Covey, K., & Stassun, K. G. 2020, *AJ*, **160**, 279
 Lallement, R., Babusiaux, C., Vergely, J. L., et al. 2019, *A&A*, **625**, A135
 Luhman, K. L. 2022, *AJ*, **163**, 24
 Mac Low, M.-M., & Klessen, R. S. 2004, *RvMP*, **76**, 125
 Marshall, P., Anguita, T., Bianco, F. B., et al. 2017, arXiv:1708.04058
 Marshall, D. J., Robin, A. C., Reylé, C., Schultheis, M., & Picaud, S. 2006, *A&A*, **453**, 635
 Minniti, D., Lucas, P. W., Emerson, J. P., et al. 2010, *NewA*, **15**, 433
 Olsen, K. A. G., Blum, R. D., & Rigaut, F. 2003, *AJ*, **126**, 452
 Parker, R. J., Wright, N. J., Goodwin, S. P., & Meyer, M. R. 2014, *MNRAS*, **438**, 620
 Planck Collaboration, Aghanim, N., Aghanim, & Ashdown, M. 2016, *A&A*, **596**, A109
 Prisinzano, L., Damiani, F., Guarcello, M. G., et al. 2018a, *A&A*, **617**, A63
 Prisinzano, L., Damiani, F., Sciortino, S., et al. 2022, *A&A*, **664**, A175
 Prisinzano, L., Magrini, L., & Damiani, F. 2018b, arXiv:1812.03025
 Reid, M. J., Menten, K. M., Brunthaler, A., et al. 2014, *ApJ*, **783**, 130
 Schlegel, D. J., Finkbeiner, D. P., & Davis, M. 1998, *ApJ*, **500**, 525
 Street, R. A., Bachelet, E., Tsapras, Y., et al. 2023, *ApJS*, submitted
 Tanaka, K. E. I., Tan, J. C., Zhang, Y., & Hosokawa, T. 2018, *ApJ*, **861**, 68
 Tassis, K., & Mouschovias, T. C. 2018, *ApJ*, **616**, 283
 Tognelli, E., Prada Moroni, P. G., & Degl'Innocenti, S. 2018, *MNRAS*, **476**, 27
 Venuti, L., Damiani, F., & Prisinzano, L. 2019, *A&A*, **621**, A14
 Weidner, C., Kroupa, P., & Bonnell, I. A. D. 2010, *MNRAS*, **401**, 275
 Zari, E., Hashemi, H., Brown, A. G. A., Jardine, K., & de Zeeuw, P. T. 2018, *A&A*, **620**, A172